Quantitative Analysis of Electron Acceleration in Coalescing Magnetic Flux Ropes at Earth's Magnetopause

Wenqing Ma[1,3], Meng Zhou[2,3]*, Zhihong Zhong[2,3]†, Xiaohua Deng[3]

[1] School of Resources and Environment, Nanchang University, Nanchang, People's Republic of China.

[2] Department of Physics, School of Physics and Materials Science, Nanchang University, Nanchang, People's Republic of China.

[3] Institute of Space Science and Technology, Nanchang University, Nanchang, People's Republic of China.

*Corresponding author: Meng Zhou (monmentum82@gmail.com)

†Corresponding author: Zhihong Zhong (zhong.zh@outlook.com)

Key Points:

- First observation of two coalescing reconnections among three magnetic flux ropes (MFRs)
- Coalescing MFRs result in greater acceleration rates and generate more suprathermal electrons than that in non-coalescing MFRs
- Fermi and $E_{\parallel}$ accelerations are the dominant mechanisms in coalescing MFRs, while $E_{\parallel}$ is the dominant mechanism in non-coalescing MFRs

Abstract

Coalescence of magnetic flux ropes (MFRs) is suggested as a crucial mechanism for electron acceleration in various astrophysical plasma systems. However, how electrons are being accelerated via MFR coalescence is not fully understood. In this paper, we quantitatively analyze electron acceleration during the coalescence of three MFRs at Earth's magnetopause using in-situ Magnetospheric Multiscale (MMS) observations. We find that suprathermal electrons are enhanced in the coalescing MFRs than those in the ambient magnetosheath and non-coalescing MFRs. Both first-order Fermi and $E_{||}$ acceleration were responsible for this electron acceleration, while the overall effect of betatron mechanism decelerated the electrons. The most intense Fermi acceleration was observed in the trailing part of the middle MFR, while $E_{||}$ acceleration occurred primarily at the reconnection sites between the coalescing MFRs. For non-coalescing MFRs, the dominant acceleration mechanism is the $E_{||}$ acceleration. Our results further consolidate the important role of MFR coalescence in electron acceleration in space plasma.

Plain Language Summary

Magnetic flux ropes are common magnetic structures in space environments and are believed to play a significant role in electron acceleration. Adjacent magnetic flux ropes can coalesce through magnetic reconnection, forming larger-scale magnetic flux ropes. The significant efficiency of electron acceleration within coalescing magnetic flux ropes has been reported thoroughly by theoretical and numerical simulation studies, but has not been confirmed by in-situ observation. Our research reports an event of three magnetic flux ropes coalescing in pairs and provides detailed quantitative analyses of associated acceleration mechanisms. Furthermore, we compare the electron accelerations within these coalescing magnetic flux ropes with other non-coalescing flux ropes. Our study contributes to a further understanding of the production mechanisms of high-energy electrons in space plasmas.

1 Introduction

Magnetic reconnection is a pervasive phenomenon in space and astrophysical plasmas, efficiently converting magnetic energy into plasma energy. Part of the magnetic energy is used to energize suprathermal particles, which has frequently been detected in space observations and numerical simulations (Coroniti & Kennel, 1972; Drake et al., 2006; Fu et al., 2006; Fu et al., 2019; Matthaeus et al., 1984; Øieroset et al., 2002; Zhou et al., 2016). High-energy particles

generated in the magnetotail may serve as seed particles for relativistic particles in the inner magnetosphere, playing a pivotal role in the dynamics of the radiation belts (Lui et al., 2012; Tang et al., 2017; Turner et al., 2021).

Magnetic flux ropes (MFRs), also known as magnetic islands, plasmoids, or flux transfer events, are helical magnetic structures commonly observed in space plasmas (Slavin et al., 2003; Zong et al., 2004). It is widely acknowledged that MFRs are by-products of magnetic reconnection, generated through tearing instability or Kelvin-Helmholtz instability (Zhong et al., 2018; Zhou et al., 2012). MFRs are considered one of the most significant structures for electron acceleration during reconnection (Drake et al., 2006; Chen et al., 2008; Retino et al., 2008; Huang et al., 2012; Zhong et al., 2020; Zhou et al., 2018). Electron acceleration within MFRs primarily involves local betatron acceleration due to the compressed core magnetic field inside the MFR (Zhong et al. 2020), first-order Fermi acceleration resulting from MFR contraction (Drake et al., 2006), parallel electric field acceleration inside and at the perimeter of the MFR (Zhou et al., 2018), island surfing acceleration (Oka et al., 2010a) and non-adiabatic turbulent acceleration mechanism (Fujimoto and Cao, 2021).

MFRs may coalesce/merge with each other to form MFRs with larger spatial size through reconnection between them (Pritchett, 2007; Wang et al., 2016a; Zhou et al., 2017). Theoretically, it has been suggested that the coalescence of magnetic islands can efficiently energize electrons, primarily through first-order Fermi acceleration and direct acceleration via the reconnection electric field at the merging site (Oka et al., 2010b; Le Roux et al., 2015; Pritchett, 2008; Wang et al., 2016b; Du et al., 2018; Li et al., 2017). Fermi acceleration results from the shrinking of magnetic field lines during the coalescence. From the perspective of single particle motion, it is due to the curvature drift along the electric field. Drake et al. (2012) propose that the first-order Fermi mechanism is more efficient during the coalescence of multiple magnetic islands than for a single MFR, and the energized particles exhibit a power-law distribution with $f \sim E^{-1.5}$.

Although theoretical and simulation studies have widely suggested that MFR coalescence can provide significant electron acceleration, there is currently a lack of in-situ observations to consolidate this scenario. In this paper, we present MMS observations of a series of MFRs in a reconnection exhaust at the magnetopause subsolar region. The first three MFRs in this series

were coalescing with each other, while the other MFRs were not. The high-resolution data recorded by the Magnetospheric Multiscale (MMS) mission (Burch et al., 2016) provides us a unique opportunity to study the electron acceleration by the coalescing MFRs and compare the degree of electron acceleration between coalescing and non-coalescing MFRs. The remainder of this paper is organized as follows: Section 2 provides the overview of the MFRs. Section 3 and Section 4 present the evidence of MFRs coalescing and electron acceleration within the MFRs. Section 5 discusses and summarizes our results.

2 Event Overview

On 2015 November 17, from 02:15:00 to 02:21:30 UT, the four MMS spacecraft traversed the subsolar magnetopause at an approximate location of [9.7, −0.9, −0.3] R_E in Geocentric Solar Magnetospheric (GSM) coordinates. The average separation between the four spacecraft was about 20 km, leading to quite similar observations from each of them. The data utilized in this study were obtained from the following instruments onboard MMS: the Fluxgate Magnetometer (FGM) (Russell et al., 2016), which provides three-dimensional magnetic field vectors; the Fast Plasma Investigator (FPI) (Pollock et al., 2016) offering plasma velocity distributions and moments; and the Electric Double Probe (EDP) (Ergun et al., 2016; Lindqvist et al., 2016; Torbert et al., 2016) provides three-dimensional electric field vectors.

Figure 1 displays an overview of the observations from MMS2 during this this time interval. Given the spacecraft's proximity to the subsolar point, the GSM coordinate system serves as a reasonable approximation to the boundary normal coordinate system of the magnetopause, as the magnetopause normal closely aligns with the GSM-x direction (e.g., Zhou et al., 2017). Multiple bipolar variations of the magnetic field B_X component are accompanied by peaks of the B_Y component and the increases in total magnetic field strength, which are typical signatures of MFRs (Figures 1(a) and 1(b)) (Zong et al., 2004). Magnetic field B_Z (Figure 1(a)) exhibits several sign reversals during this period, indicating that MMS repeatedly crossed the magnetopause between the magnetosphere (B_Z >0) and magnetosheath (B_Z <0). These MFRs were embedded in two large southward bulk flows driven by reconnection (Figures 1(c) and 1(d)) within the magnetopause boundary layer (Zhou et al., 2017). These two flows were separated by a quiescent flow period, occurring from approximately 02:18:30 UT to 02:19:30 UT. Ions and electrons from both the magnetosphere and the magnetosheath mixed within this

reconnection outflow, a clear indication of an opening magnetopause. Our focus will be on the three consecutive MFRs observed between 02:15:10 and 02:17:20 UT, marked by the magenta rectangle in Figure 1.

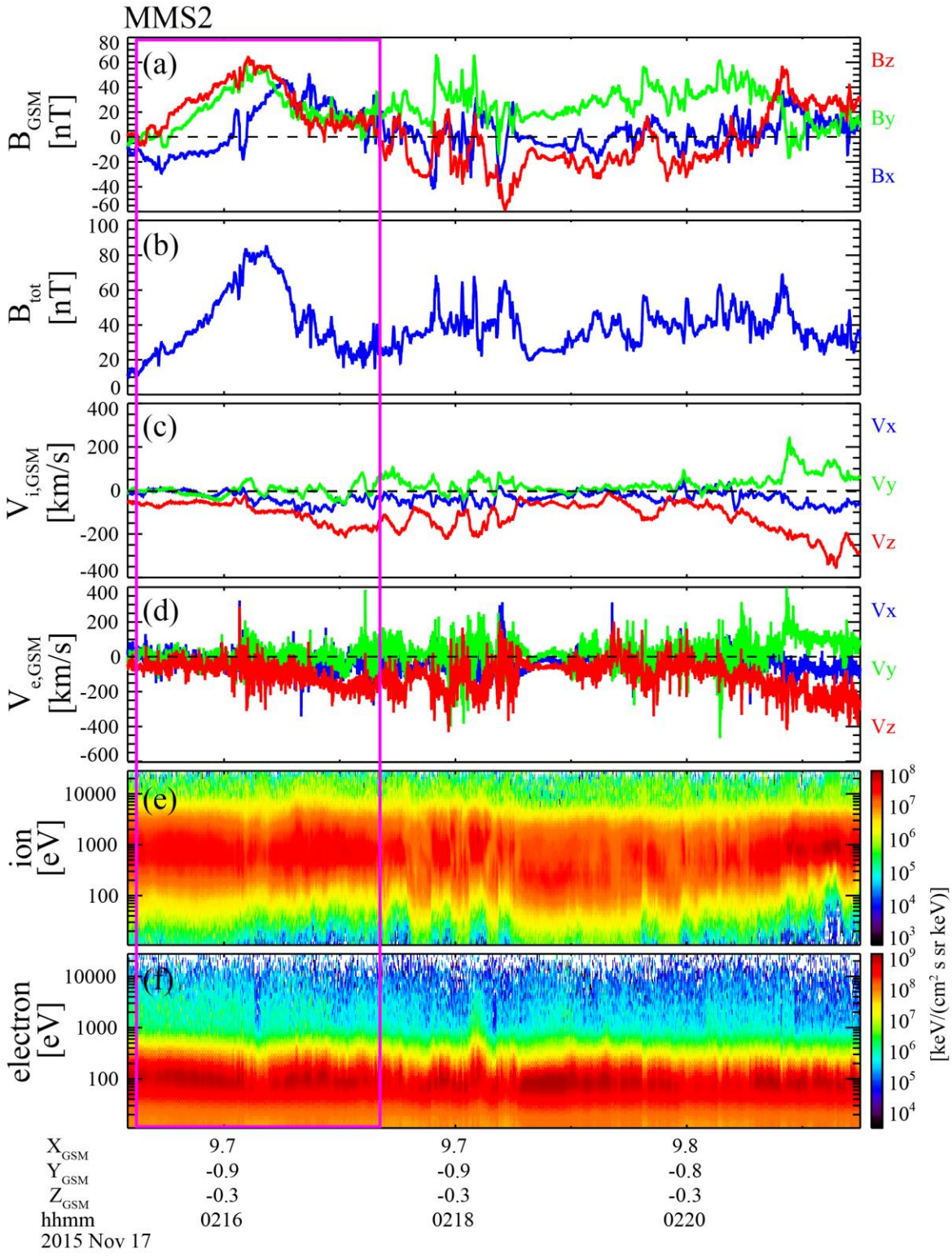

Figure 1. Overview of MMS2 observations between 02:15:00 and 02:21:30 UT. From the top to bottom are: (a) magnetic field vectors; (b) magnetic field strength; (c) ion bulk velocity; (d) electron bulk velocity; (e) ion and (f) electron omni-directional differential energy fluxes. All vectors are presented in GSM coordinates. The magenta rectangle highlights the observations of the three coalescing MFRs.

3 Electron Acceleration within Coalescing MFRs

Figures 2(a)-(f) present observations from 02:15:10 UT to 02:17:21 UT, during which the three consecutive MFRs were observed by MMS. Zhou et al. (2017) reported the merging of the first two large-scale MFRs, with an electron diffusion region identified between MFR1 and MFR2. Here we unveil another smaller MFR (denoted as MFR3), which was adjacent to the tail of MFR2, merging with MFR2. The three MFRs were identified as quasi-2D structures based on the minimum directional derivative (MDD) analysis (Shi et al., 2005) because $\lambda_1 \sim \lambda_2 >> \lambda_3$, where the three eigenvalues λ_1, λ_2, and λ_3 represent the maximum, intermediate and minimum values of the magnetic field directional derivatives. The 2-D structure velocities calculated by the spatio-temporal difference method (Shi et al., 2006) using the magnetic field data smoothed to the resolution of 0.03 s are depicted in Figure 2(e). One can see that the structure velocities closely match both the ion (Figure 2(c)) and electron bulk velocities (Figure 2(d)). Considering the moving velocities and the observational durations of the MFRs, we estimate the cross-section sizes of MFR1, MFR2, and MFR3 as approximately ~ 59 d_i, ~ 145 d_i, and ~ 15 d_i, respectively, with d_i being the ion inertial length, around 42 km, given an average number density of ~30 cm^{-3}.

Interestingly, we note that a high-speed electron jet in the Y direction was observed between MFR2 and MFR3 (the orange shading in Figures 2(a)-(f)). To further understand the nature of this electron jet, we investigate the details of this electron jet in the local boundary normal (LMN) coordinates (shown in Figures 2(g)-(n)). The transformation from GSM to LMN coordinates constructed by the minimum variance analysis (Sonnerup & Scheible, 1998) is given by: **L** = (0.778, -0.564, 0.276), **M** = (0.431, 0.799, 0.419), **N** = (-0.457, -0.207, 0.865), where **N** is the normal of the current sheet corresponding to the jet, **L** is the eigenvector of the maximum eigenvalue, and **M** completes the right-handed orthogonal coordinate system, i.e., **M** = **N** × **L**. Figure 2(g) illustrates that a reversal of B_L corresponds to a large out-of-plane current in the -**M** direction with a peak value of approximately 2,200 nA/m^2 (Figure 2(i)). This current is highly

anticorrelated to electron flow, indicating that it is predominantly carried by electrons (the V_{eM} peak ~ -340 km/s in Figure 2(h)). V_{eL} exhibits a tripolar variation relative to the background velocity V_L, approximately -100 km/s, during the current sheet crossing. After removing the background velocity, the peak value of V_{eL} is around 100 km/s, surpassing the asymptotic Alfven speed of this current sheet. Figures 3(j)-(l) show the three components of the measured electric field **E**, convective electric fields for ions and electrons, i.e., $-\mathbf{V}_i\times\mathbf{B}$, and $-\mathbf{V}_e\times\mathbf{B}$. We see that both $-\mathbf{V}_i\times\mathbf{B}$ and $-\mathbf{V}_e\times\mathbf{B}$ deviate from **E** in the current sheet, suggesting the decoupling of ions and electrons from the magnetic field in this region. This results in a peak energy dissipation $\mathbf{J}\cdot\mathbf{E}' \sim 4$ nW/m^3 at the center of the current sheet (Figure 2(m)). In Figure 2(n), a prominent peak in the electron non-gyrotropy measurement $\sqrt{Q}$ inside the current sheet (Swisdak, 2016) is evident. The peak value of $\sqrt{Q} \sim 0.04$ is about 4 times larger than the background value ~ 0.01. The above evidences strongly support that MMS encountered a reconnecting current sheet between MFR2 and MFR3. The direction of current J_M is consistent with the coalescence of two MFRs rather than the splitting of a larger MFR into two smaller MFRs (Zhong et al., 2023). Consequently, we deduce that MMS observed three contiguous MFRs coalescing in pairs at the dayside magnetopause. The average structure velocities for MFR3 and MFR2 were 125 km/s and 92 km/s, respectively, suggesting that the coalescence happened because MFR3 caught up with MFR2.

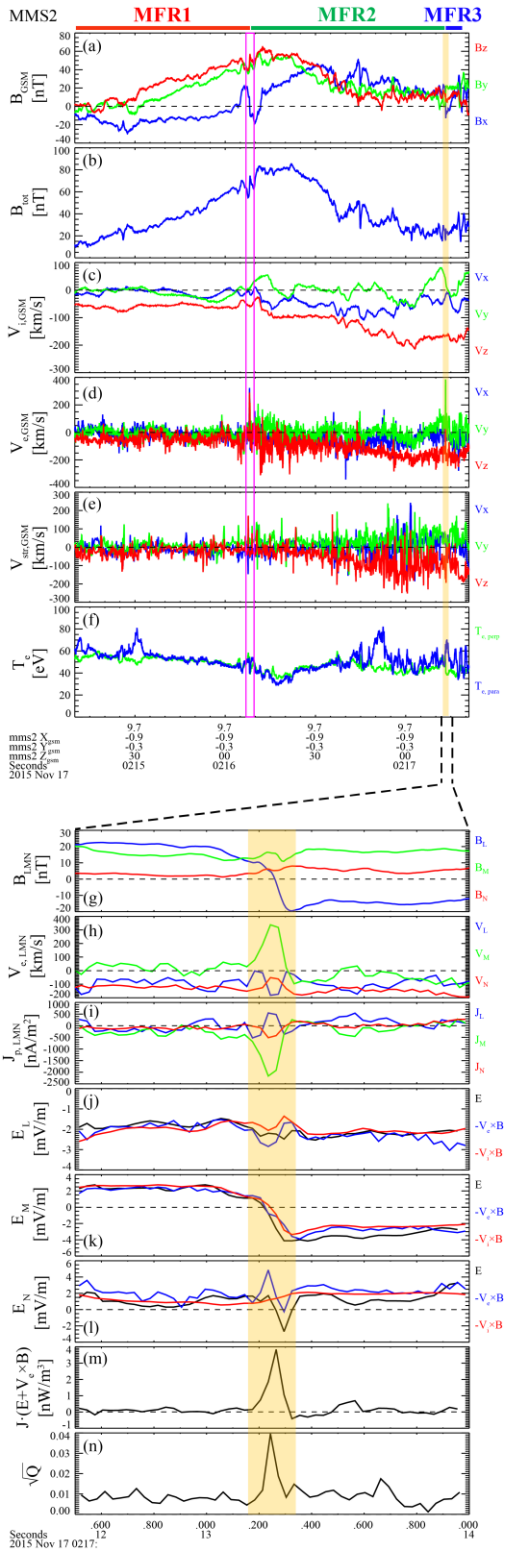

Figure 2. The top column shows the observation of the first three MFRs in GSM coordinates: (a) magnetic field vectors, (b) magnetic field strength, (c) ion bulk velocity, (d) electron bulk velocity, (e) magnetic structure velocity estimated by STD method, (f) electron parallel (blue)

and perpendicular temperatures (green). The bottom column displays the observations of the reconnecting current sheet between MFR2 and MFR3 in LMN coordinates: (g) magnetic field vectors, (h) electron bulk velocity, (i) current density, (j) – (l) three components of the measured electric field (black), $-\mathbf{V}_e\times\mathbf{B}$ (blue), and $-\mathbf{V}_i\times\mathbf{B}$ (red), (m) energy dissipation $\boldsymbol{J}\cdot\boldsymbol{E}'=\boldsymbol{J}\cdot(\boldsymbol{E}+\boldsymbol{V}_e\times\boldsymbol{B})$, (n) electron non-gyrotropy measurement $\sqrt{Q}$. The orange shading marks the reconnecting current sheet between MFR2 and MFR3.

Below we quantitatively evaluate the electron acceleration associated with the three coalescing MFRs. In principle, the first-order acceleration of a well-magnetized particle includes Fermi, betatron mechanism, and direct acceleration by parallel electric field (e.g., Northrop, 1963). The bulk acceleration rates of the first-order Fermi, betatron, and $E_{||}$ mechanism can be estimated using the following formulas (Dahlin et al. 2014; Akhavan-Tafti et al., 2019; Ma et al. 2020, 2022; Xu et al., 2023; Zhong et al. 2020):

$$W_{Fermi}=(P_{e||}+n_e m_e v_{||}^2)\vec{v}_{E\times B}\cdot(\vec{b}\cdot\nabla\vec{b}) \quad (1)$$

$$W_{betatron}=P_{e\perp}\vec{v}_{E\times B}\cdot\frac{\nabla B}{B}+\frac{P_{e\perp}}{B}\frac{\partial B}{\partial t} \quad (2)$$

$$W_{E||}=J_{e||}E_{||}+\frac{\beta_\perp}{2}J_{||}E_{||} \quad (3)$$

where P_e is the electron pressure, n_e is the electron density, $\beta_\perp$ is defined as the perpendicular plasma pressure divided by the magnetic pressure: $\beta_\perp=\frac{P_\perp}{B^2/2\mu_0}$, $J_{e||}$ is the electron parallel current, and $J_{||}$ is the total parallel current. Equations (1)-(3) demonstrate the amount of electron energy gained per unit volume per unit time through the three mechanisms. The bulk acceleration rates of the three acceleration mechanisms within the merging MFRs are presented in Figures 3(a)-(i). Note that the applicability of these formulas requires the motion of electrons to satisfy the guiding center approximation (Northrop 1963). We employ the κ value to evaluate electron adiabatic motion and determine if the guiding center approximation has been satisfied. The κ value is defined as follows (Büchner & Zelenyi 1989):

$$\kappa=\sqrt{R_C/R_L} \quad (4)$$

where R_C and R_L represent the magnetic field curvature radius and the electron Larmor radius, respectively. A large κ typically corresponds to a magnetized orbit of particles.

Figure 3(b) exhibits the κ value of electrons with energy four times the electron temperature, encompassing the energy range of most electrons (Ma et al., 2020; Xu et al., 2023). Throughout the entire interval, the κ value consistently exceeds 3, indicating that electrons satisfy the guiding center approximation within the three MFRs, allowing for the quantification of their bulk acceleration using Eqs. (1)-(3). We see that the bulk Fermi acceleration rate exhibits large fluctuations within MFR3, the trailing part of MFR2 and the leading edge of MFR1 (Figure 3c). The positive peak value reaches about 4,000 eV/s/cm^3. Figure 3(e) reveals that the betatron acceleration rate exhibits several significant peaks in the leading part of MFR1, the trailing part of MFR2, and throughout MFR3. Specifically, a considerable positive peak of ~ 2,200 eV/s/cm^3 occurs in the reconnection region between MFR1 and MFR2; along with a significant positive peak of ~ 5,000 eV/s/cm^3, accompanied by a conspicuous negative peak of approximately -9,000 eV/s/cm^3, appearing in the reconnection region of MFR2 and MFR3. The $E_{\parallel}$ acceleration rate, illustrated in Figure 3(g), displays several extremely large positive peaks exceeding 10,000 eV/s/cm^3, surpassing the peak values of both the Fermi and betatron acceleration rates. These prominent peaks and disturbances of the $E_{\parallel}$ acceleration rate primarily manifest within and around the two reconnection regions.

To assess the net effects of the three mechanisms, we calculate the spatial integral of the acceleration rates by the following formula:

$$W_S = \int W v_{str} dt \qquad (5)$$

where W is the local acceleration rate, and v_{str} is the structure velocity as shown in Figure 2(e). The rising trend of W_S marks the acceleration region, while the downtrend denotes the deceleration region. In Figures 3(d), 3(f), 3(h), and 3(i), the spatial integrals of the Fermi, betatron, and $E_{\parallel}$ mechanisms, along with the total acceleration rate (the sum of the rates from the three different mechanisms), are presented. It is evident that the Fermi mechanism primarily functions as a decelerator in MFR1 and the leading edge of MFR3 (Figure 3(d)), while it is negligible in the leading part of MFR2 and the center of MFR3. Whereas, it shows a significant net increase in the trailing part of MFR2 and a weak enhancement in the trailing edge of MFR3. These features are different from the Fermi acceleration within a single FR in which Fermi acceleration is typically negative on one side of the MFR and positive on the other side (Zhong et al., 2020; Jiang et al., 2021). The intense Fermi acceleration in the trailing part of MFR2 is

probably due to the contraction of the helical magnetic field lines carried by the large bulk flow at the trailing edge of MFR2.

Figure 3(f) reveals that betatron acceleration primarily takes place in and around the coalescing region between MFR1 and MFR2, the central area of the newly formed large MFR. Conversely, betatron cooling predominantly occurs within the coalescing region between MFR2 and MFR3. This implies that the coalescence of two large MFRs results in significant betatron acceleration, while the merging between the large MFR and the small MFR results in betatron cooling. One of the most notable distinctions between the two coalescences is the strength of the core field. The core field (contributed by B_Y and B_Z) in the coalesced MFR between MFR1 and MFR2 significantly surpasses the reconnecting field B_X. The contraction of the newly formed MFR from MFR1 and MFR2 could lead to an increase in the core field, which exceeds the decrease of B_x due to reconnection, hence resulting in betatron acceleration. In contrast, the coalescence of MFR2 and MFR3 fails to produce a core field with sufficient strength to counterbalance the diminished magnetic field due to reconnection, which results in the magnetic field decrease and betatron cooling.

Figure 3(h) illustrates that $E_{\parallel}$ acceleration typically experiences abrupt changes within several narrow regions, indicating that $E_{\parallel}$ acceleration and deceleration are more localized compared to Fermi and betatron acceleration. Particularly, we note that the acceleration from $E_{\parallel}$ is the most intense in the vicinity of the reconnection sites (the magenta regions in Figure 3). These indicate that the acceleration from $E_{\parallel}$ plays a more critical role in the central region of the coalesced MFRs, which is different from the previous results suggesting that $E_{\parallel}$ acceleration mainly occurs at the MFR edges in the single MFR scenario (Zhou et al., 2018; Akhavan-Tafti et al., 2019).

Figure 3(i) displays the spatial integral of the total acceleration rate, demonstrating the collective impact of the three mechanisms within these coalescing MFRs. The total integrated rate increases significantly around the reconnection region, as well as at the trailing edges of MFR2 and MFR3, which are highlighted by the magenta dashed box in Figure 3. These areas represent the major acceleration regions in the coalescing MFRs. The primary acceleration mechanisms in these acceleration regions are the Fermi mechanism and the $E_{\parallel}$ mechanism. The maximum integrated values of the two mechanisms are almost identical. The relative positions of the three MFRs and the associated acceleration regions are depicted in Figure 4.

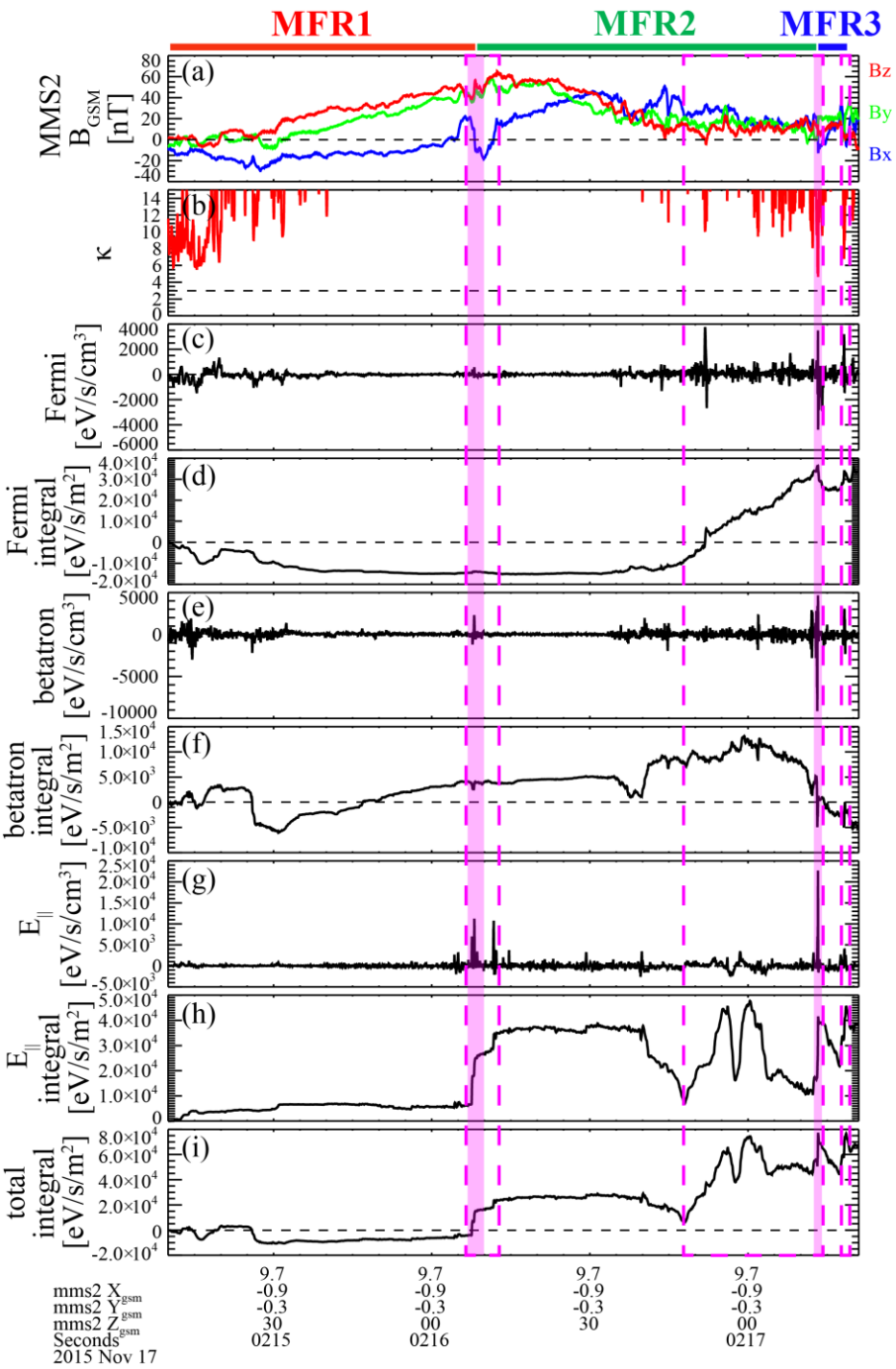

Figure 3. Electron acceleration condition in the MFRs, (a) magnetic field vectors, (b) the κ value for electrons calculated by 2 times of thermal speed, (c) local Fermi acceleration rate, (d) the spatial integral of Fermi acceleration rate, (e) local and (f) the spatial integral of betatron acceleration rate, (g) local and (h) the spatial integral of the $E_{||}$ acceleration rate, (i) the spatial integral of the total acceleration rate. The magenta shaded areas represent the reconnection regions, while the magenta dashed boxes encircle the primary acceleration regions.

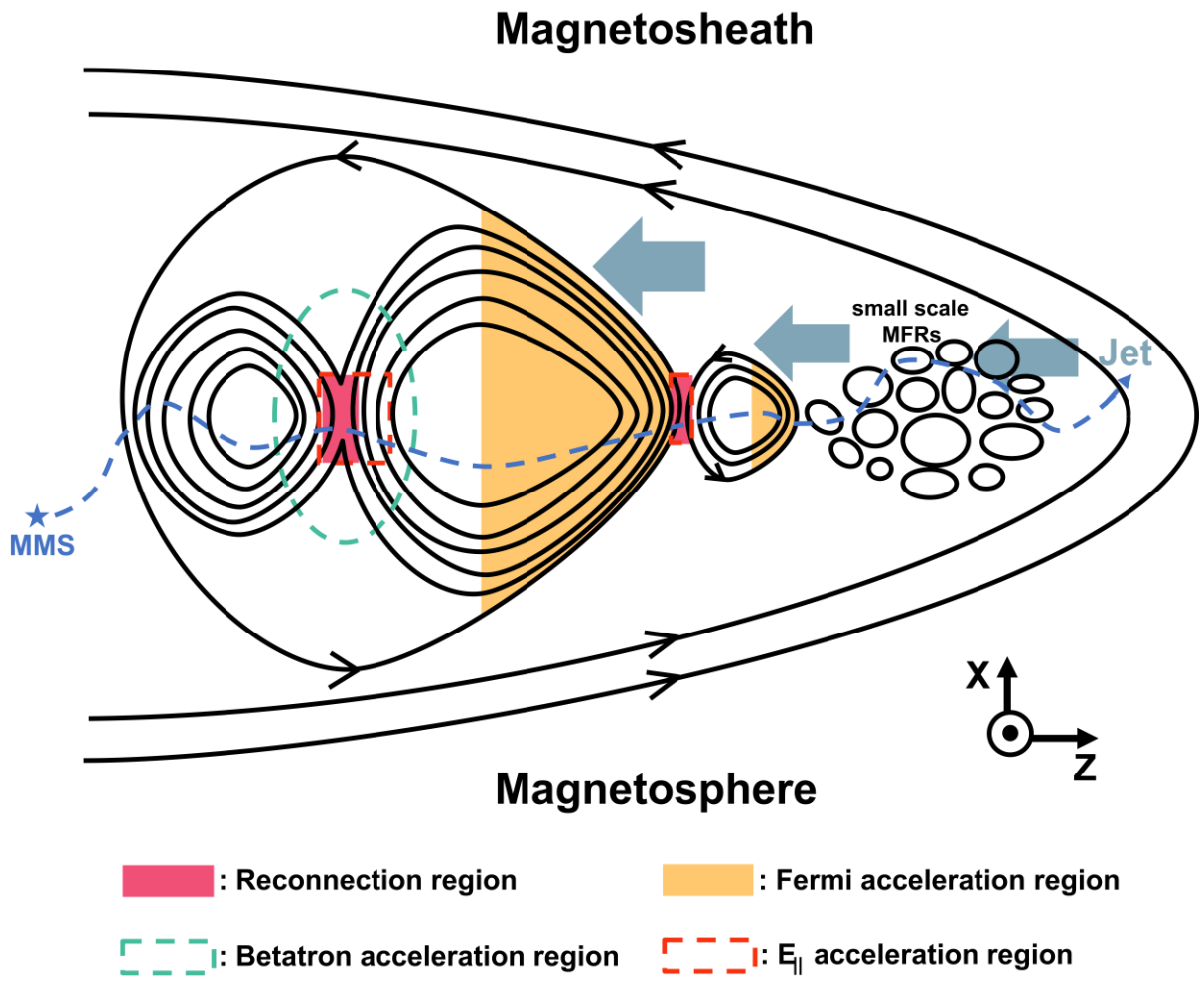

Figure 4. A schematic view of the three MFRs with the associated acceleration region. The dashed curve represents the surmised MMS trajectory across these MFRs.

4 Comparison between Coalescing and Non-coalescing MFRs

Figure 1 illustrates the presence of a series of short-period MFRs observed from 02:17:25 to 02:21:26 UT, occurring after the observation of the three coalescing MFRs. We do not find clear signatures of coalescence between these MFRs, i.e., no obvious current sheets and energy dissipation observed at their edges, thereby we call them non-coalescing MFRs in the following. We have identified 14 non-coalescing MFRs during this interval in total. The cross-section sizes of these small-scale MFRs are from 6 d_i to 48 d_i, which are derived through the same analysis to infer the cross-section sizes of the three coalescing MFRs as we mentioned in the former section.

Subsequently, we compare the electron acceleration associated with these small-scale MFRs to that associated with the coalescing MFRs.

Figure 5 presents the ratio *R* between the phase space density (PSD) in the MFRs and the PSD in the magnetosheath for a given energy *W*. *R* is defined as

$$R(W) = \frac{PSD_{MFR}(W) - PSD_{sheath}(W)}{PSD_{sheath}(W)} \quad (6).$$

The magnetosheath reference interval is selected from 03:40:00 to 03:50:00 UT (not shown). Since the reference interval of magnetosheath lacks burst mode FPI data, *R* in Figure 5 is calculated using the fast mode data with a time resolution of 4.5 s. The average PSD within small-scale non-coalescing MFRs is calculated from FPI fast mode data between 02:17:25 and 02:21:26 UT, during which 14 MFRs were observed sequentially. For energetic electrons (> 1,000 eV), the values of *R* are close to 0 (Figure 5), indicating that there were almost no magnetospheric energetic electrons in the MFRs. Therefore, the electrons within these MFRs primarily originated from the magnetosheath. It's noteworthy that *R* is below 0 for all MFRs when the energy is below 100 eV, whereas *R* becomes positive in the 100-1,000 eV range. This implies that low-energy (< 100 eV) electrons may experience localized acceleration to higher energy in both coalescing and non-coalescing MFRs. The peaks in *R* are consistently near 300 eV, which is nearly six times the electron temperature of approximately 50 eV. This suggests that the acceleration within these MFRs results in the production of suprathermal electrons. *R* of MFR1 exhibits the highest peak of ~7.5 while R corresponding to small-scale non-coalescing MFRs has the lowest peak of ~ 1.5. Therefore, the production of suprathermal electrons is more significant in coalescing MFRs compared to non-coalescing ones.

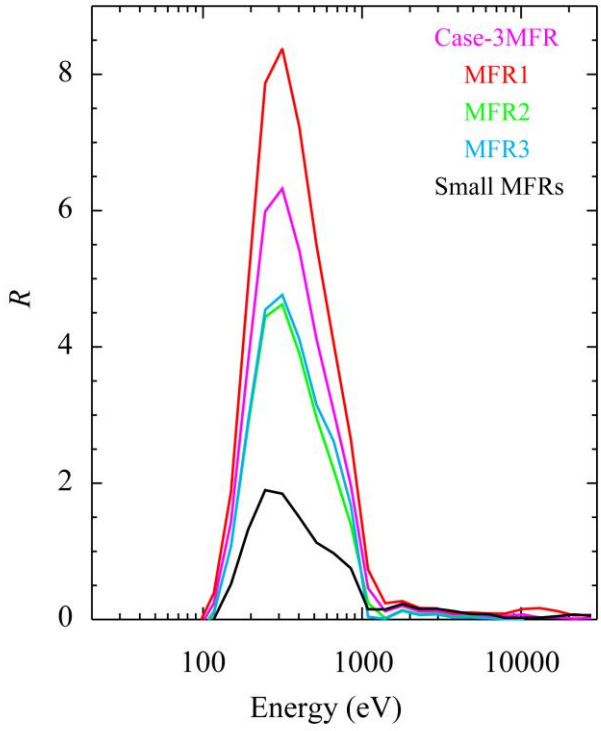

Figure 5. The ratio *R* within the three coalescing MFRs (magenta), MFR1 (red), MFR2 (green), MFR3 (blue), and small-scale MFRs (black).

We performed a Liouville mapping by setting the magnetosheath electrons as the source electrons and compared the PSDs in the MFRs to the analytically derived PSD accelerated from the source. We found that R=7.5 in the suprathermal energy range is roughly equivalent to an adiabatic acceleration factor of 1.3. In other words, there is a 1.3 times enhancement of |B| or shrinking of field lines in which the electrons are trapped by a factor of 1.3 (Fu et al., 2013). If the electrons are predominantly accelerated by $E_{||}$, then an R value of 7.5 corresponds to a parallel potential of approximately 100 V, which is equivalent to a 100 eV increase in electron energy. This degree of acceleration is comparable to the electron acceleration associated with magnetopause reconnection (Graham et al., 2016) and dipolarization fronts in the magnetotail (Fu et al., 2013).

Figure 6 provides a comparison of spatially integrated acceleration rates within the coalescing MFRs and non-coalescing MFRs. The magenta, green, and blue dots in Figure 6 represent the rates within each coalescing MFR, the black dot symbolizes the average rate across the three coalescing MFRs, and the red dots represent the rates within each non-coalescing MFR. An

observation is evident that the integrated betatron acceleration rate is consistently close to zero in all MFRs. The integrated Fermi acceleration rate is near zero in most of the non-coalescing MFRs. However, it is noteworthy that four non-coalescing MFRs exhibit substantial values ranging between (1.0 - 2.5) × 10^4 eV/s/m^2. Particularly, in MFR2, the integrated Fermi acceleration rate reaches approximately 5×10^4 eV/s/m^2 (indicated by the green dot in Figure 6(a)), which is larger than the values observed in all non-coalescing MFRs. This contributes to a higher average Fermi acceleration rate within the coalescing MFRs, denoted by the black dot in Figure 6(a). Figure 6(b) further compares the integrated Fermi acceleration rate with the $E_{\parallel}$ acceleration rate in each MFR. It is evident that the integrated $E_{\parallel}$ acceleration rate is typically larger than the Fermi acceleration in the non-coalescing MFRs, whereas it is nearly equivalent to the integrated Fermi acceleration rate in the coalescing MFRs. Figure 6(c) reveals that the betatron acceleration rate is generally smaller than the $E_{\parallel}$ acceleration rate in all MFRs. This implies that the net Fermi and betatron accelerations in these non-coalescing MFRs are generally weak, whereas $E_{\parallel}$ acceleration is the primary mechanism responsible for electron acceleration in the non-coalescing MFRs. Moreover, the integrated Fermi acceleration rate in coalescing MFRs is larger than that in non-coalescing MFRs.

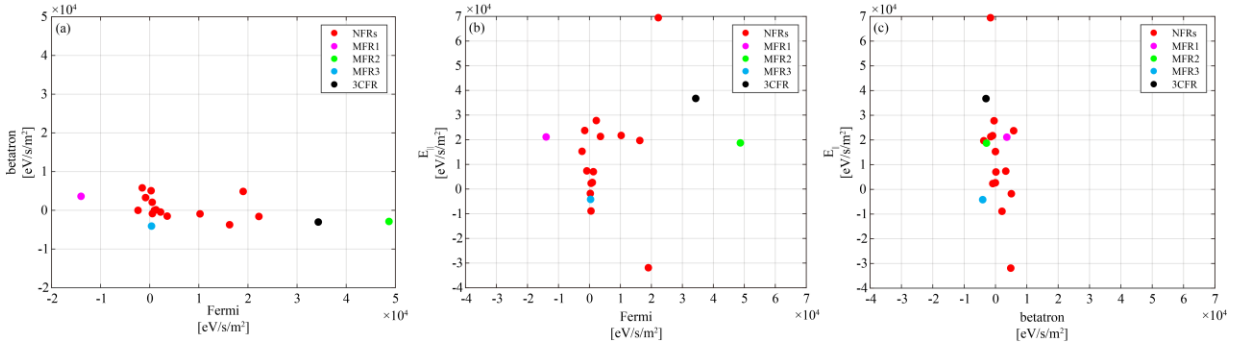

Figure 6. (a) – (c) Scatter plots of the spatial integrated acceleration rates inside MFRs. Red, magenta, green, blue, and black dots represent the results of the non-coalescing MFRs (NFRs), MFR1, MFR2, MFR3, and the three coalescing MFRs as a whole (3CFR), respectively.

Table 1 provides a breakdown of the percentage of primary acceleration mechanisms within non-coalescing MFRs. The dominant acceleration mechanism is determined based on the largest integrated acceleration rate within a single MFR. It should be noted that the negative value is consistently smaller than the positive value. We find that $E_{\parallel}$ acceleration accounts for the largest percentage, ~ 78.6%, signifying that $E_{\parallel}$ acceleration is the predominant mechanism in 11 out of

14 non-coalescing MFRs. We also find that Fermi process is the dominant mechanism in none of the non-coalescing MFRs, which is distinct from that in the coalescing MFRs. There are also two non-coalescing MFRs in which the total acceleration rate is negative.

Table 1

Major Acceleration Mechanism and its Percentage in Non-coalescing MFRs

Major acceleration mechanism	Number of NFRs (14 in total)	Percentage
Fermi	0	0%
betatron	1	7.1%
$E_{\parallel}$	11	78.6%
No acceleration*	2	14.3%

Note. The major acceleration mechanism means the one with the largest integrated rate.

*"No acceleration" means that the integrated total acceleration rate is negative.

Table 2 presents the percentage of acceleration (positive value) and deceleration (negative value) effects for the three mechanisms within these non-coalescing MFRs. It is observed that Fermi acceleration occurs in 11 out of 14 non-coalescing MFRs, while Fermi deceleration is observed in 3 out of 14 non-coalescing MFRs. A similar percentage applies to $E_{\parallel}$ acceleration and deceleration, indicating that both the Fermi and $E_{\parallel}$ mechanisms primarily contribute to electron acceleration rather than deceleration in most non-coalescing MFRs. However, it is worth noting that, as indicated by the red dots in Figure 6(b), the integrated Fermi acceleration rate in most non-coalescing MFRs is typically close to zero, significantly smaller than the integrated $E_{\parallel}$ acceleration rate. Additionally, the percentage of betatron acceleration is smaller than that of betatron cooling.

Table 2

A statistic of acceleration and deceleration effects of each mechanism in non-coalescing MFRs

Acceleration mechanism	Positive/acceleration percentage (number)	Negative/deceleration percentage (number)
Fermi	78.6% (11)	21.4% (3)

betatron	42.9% (6)	57.1% (8)
$E_{\parallel}$	78.6% (11)	21.4% (3)

5 Summary

In summary, our study presents a quantitative analysis of electron acceleration within a series of MFRs located in a reconnection exhaust at the subsolar magnetopause. These MFRs can be classified into two distinct categories: coalescing MFRs and non-coalescing MFRs. Our investigation also involves a comparative assessment of electron acceleration between these two types of MFRs. The major findings can be summarized as follows:

1. MMS observed two MFR coalescences among three MFRs, akin to a rear-end collision where the faster-moving MFR caught up with the slower one. The first coalescence involved two large-scale MFRs characterized by a strong core field (Zhou et al., 2017), while the second coalescence occurred between a large-scale MFR and a small-scale MFR with a relatively weaker core field.

2. Coalescing MFRs generated a higher population of suprathermal electrons compared to non-coalescing MFRs, consistent with the observed greater acceleration rates within coalescing MFRs.

3. The primary electron acceleration mechanisms differed between the coalescing and non-coalescing MFRs. In coalescing MFRs, Fermi and $E_{\parallel}$ mechanisms were prominent, with $E_{\parallel}$ acceleration being the dominant process in non-coalescing MFRs. Notably, in coalescing MFRs, active $E_{\parallel}$ acceleration was concentrated in the proximity of the reconnection site, and it exhibited a more localized nature compared to Fermi acceleration. These findings highlight that MFR coalescence significantly enhances the efficiency of Fermi acceleration due to field line contraction. Conversely, the relatively weak contraction in non-coalescing MFRs restricts the effectiveness of Fermi acceleration.

4. Although the integrated betatron acceleration rate was negative in both coalescing and non-coalescing MFRs, it was positive in the merging region between the two large-scale MFRs, corresponding to the compression of the large core field and enhanced electron flux around a 90° pitch angle, as previously reported by Zhou et al. (2017).

Acknowledgments

We appreciate the MMS teams for the high-quality data and successful operation. This work is supported by the National Natural Science Foundation of China (NSFC) under grants No. 42074197, 42130211, and 42104156. Z.H.Z is supported by the China Postdoctoral Science Foundation grants No. 2021M691395 and 2023T160288, and the Natural Science Foundation of Jiangxi Province grant No. 20224BAB211021.

Data Availability Statement

The data used in this study was obtained from the MMS Science Data Center (https://lasp.colorado.edu/mms/sdc/public/about/browse-wrapper/).

References

Akhavan-Tafti, M., Slavin, J. A., Sun, W. J., Le, G., & Gershman, D. J. (2019), MMS observations of plasma heating associated with FTE growth. *Geophysical Research Letters*, *46*(22), 12654-12664. doi: 10.1029/2019GL084843

Burch, J. L., Moore, T. E., Torbert, R. B., & Giles, B. (2016). Magnetospheric multiscale overview and science objectives. *Space Science Reviews*, *199*(1), 5-21. doi: 10.1007/s11214-015-0164-9

Büchner, J., & Zelenyi, L. M. (1989). Regular and chaotic charged particle motion in magnetotaillike field reversals: 1. Basic theory of trapped motion. *Journal of Geophysical Research: Space Physics*, *94*(A9), 11821-11842. doi: 10.1029/JA094iA09p11821

Chen, L. J., Bhattacharjee, A., Puhl-Quinn, P. A., Yang, H., Bessho, N., Imada, S., et al. (2008). Observation of energetic electrons within magnetic islands. *Nature Physics, 4*(1), 19-23. doi: 10.1038/nphys777

Coroniti, F. V., & Kennel, C. F. (1979, November). Magnetospheric reconnection, substorms, and energetic particle acceleration. *AIP Conference Proceedings, American Institute of Physics*, *56*(1): 169-178. doi: 10.1063/1.32078

Dahlin, J. T., Drake, J. F., & Swisdak, M. (2014). The mechanisms of electron heating and acceleration during magnetic reconnection. *Physics of Plasmas, 21*(9), 092304. doi: 10.1063/1.4894484

Drake, J. F., Shay, M. A., Thongthai, W., & Swisdak, M. (2005). Production of energetic electrons during magnetic reconnection. *Physical Review Letters, 94*(9), 095001. doi: 10.1103/PhysRevLett.94.095001

Drake, J. F., Swisdak, M., Che, H., & Shay, M. A. (2006). Electron acceleration from contracting magnetic islands during reconnection. *Nature, 443*(7111), 553-556. doi: 10.1038/nature05116

Drake, J. F., Swisdak, M., & Fermo, R. (2012). The power-law spectra of energetic particles during multi-island magnetic reconnection. *The Astrophysical Journal Letters*, *763*(1), L5. doi: 10.1088/2041-8205/763/1/L5

Du, S., Zank, G. P., Guo, F., Li, X., & Stanier, A. (2018, October). Particle Acceleration in Interacting Magnetic Flux Ropes. *Journal of Physics: Conference Series*. *IOP Publishing*, *1100*(1): 012009. doi: 10.1088/1742-6596/1100/1/012009

Eastwood, J. P., Phan, T. D., Fear, R. C., Sibeck, D. G., Angelopoulos, V., Øieroset, M., & Shay, M. A. (2012). Survival of flux transfer event (FTE) flux ropes far along the tail magnetopause. *Journal of Geophysical Research: Space Physics*, *117*(A8). doi: 10.1029/2012JA017722

Ergun, R. E., Tucker, S., Westfall, J., Goodrich, K. A., Malaspina, D. M., Summers, D., et al. (2016). The axial double probe and fields signal processing for the MMS mission. *Space Science Reviews*, *199*(1), 167-188. doi: 10.1007/s11214-014-0115-x

Fu, H. S., Khotyaintsev, Y. V., Vaivads, A., Retinò, A., & André, M. (2013). Energetic electron acceleration by unsteady magnetic reconnection. *Nature Physics*, *9*(7), 426-430. doi: 10.1038/nphys2664

Fu, H. S., Xu, Y., Vaivads, A., & Khotyaintsev, Y. V. (2019). Super-efficient electron acceleration by an isolated magnetic reconnection. *The Astrophysical Journal Letters*, *870*(2), L22. doi: 10.3847/2041-8213/aafa75

Fujimoto, K., & Cao, J. B. (2021). Non-adiabatic electron heating in the magnetic islands during magnetic reconnection. *Geophysical Research Letters*, *48*(19), e2021GL094431. doi: 10.1029/2021GL094431

Graham, D. B., Khotyaintsev, Y. V., Norgren, C., Vaivads, A., André, M., Lindqvist, P. A., et al. (2016). Electron currents and heating in the ion diffusion region of asymmetric reconnection. *Geophysical Research Letters*, *43*(10), 4691-4700. doi: 10.1002/2016GL068613

Jiang, K., Huang, S. Y., Yuan, Z. G., Deng, X. H., Wei, Y. Y., Xiong, Q. Y., et al. (2021). Statistical properties of current, energy conversion, and electron acceleration in flux ropes in the terrestrial magnetotail. *Geophysical Research Letters*, *48*(11), e2021GL093458. doi: 10.1029/2021GL093458

Le Roux, J. A., Zank, G. P., Webb, G. M., & Khabarova, O. (2015). A kinetic transport theory for particle acceleration and transport in regions of multiple contracting and reconnecting inertial-scale flux ropes. *The Astrophysical Journal*, *801*(2), 112. doi: 10.1088/0004-637X/801/2/112

Li, Y., Wu, N., & Lin, J. (2017). Charged-particle acceleration in a reconnecting current sheet including multiple magnetic islands and a nonuniform background magnetic field. *Astronomy & Astrophysics*, *605*, A120. doi: 10.1051/0004-6361/201630026

Lindqvist, P. A., Olsson, G., Torbert, R. B., King, B., Granoff, M., Rau, D., et al. (2016). The spin-plane double probe electric field instrument for MMS. *Space Science Reviews*, *199*(1), 137-165. doi: 10.1007/s11214-014-0116-9

Lui, A. T. Y., Zong, Q. G., Wang, C., & Dunlop, M. W. (2012). Electron source associated with dipolarization at the outer boundary of the radiation belts: Non-storm cases. *Journal of Geophysical Research: Space Physics*, *117*(A10). doi: 10.1029/2012JA018084

Ma, W., Zhou, M., Zhong, Z., & Deng, X. (2020). Electron acceleration rate at dipolarization fronts. *The Astrophysical Journal*, *903*(2), 84. doi: 10.3847/1538-4357/abb8cc

Ma, W., Zhou, M., Zhong, Z., & Deng, X. (2022). Contrasting the mechanisms of reconnection-driven electron acceleration with in situ observations from MMS in the terrestrial magnetotail. *The Astrophysical Journal*, *931*(2), 135. doi: 10.3847/1538-4357/ac6be6

Matthaeus, W. H., Ambrosiano, J. J., & Goldstein, M. L. (1984). Particle acceleration by turbulent magnetohydrodynamic reconnection. *Physical review letters*, *53*(15), 1449. doi: 10.1103/PhysRevLett.53.1449

Northrop, T. G. (1963). Adiabatic charged-particle motion. *Reviews of Geophysics*, *1*(3), 283-304. doi: 10.1029/RG001i003p00283

Øieroset, M., Lin, R. P., Phan, T. D., Larson, D. E., & Bale, S. D. (2002). Evidence for Electron Acceleration up to∼ 300 k e V in the Magnetic Reconnection Diffusion Region of Earth's Magnetotail. *Physical Review Letters*, *89*(19), 195001. doi: 10.1103/PhysRevLett.89.195001

471 Oka, M., Fujimoto, M., Shinohara, I., & Phan, T. D. (2010a). “Island surfing” mechanism of
472 electron acceleration during magnetic reconnection. *Journal of Geophysical Research: Space*
473 *Physics*, *115*(A8). doi: 10.1029/2010JA015392
474 Oka, M., Phan, T. D., Krucker, S., Fujimoto, M., & Shinohara, I. (2010b). Electron acceleration
475 by multi-island coalescence. *The Astrophysical Journal*, *714*(1), 915. doi: 10.1088/0004-
476 637X/714/1/915
477 Pollock, C., Moore, T., Jacques, A., Burch, J., Gliese, U., Saito, Y., et al. (2016). Fast plasma
478 investigation for magnetospheric multiscale. *Space Science Reviews*, *199*(1), 331-406. doi:
479 10.1007/s11214-016-0245-4
480 Pritchett, P. L. (2007). Kinetic properties of magnetic merging in the coalescence process.
481 *Physics of plasmas*, *14*(5), 052102. doi: 10.1063/1.2727458
482 Pritchett, P. L. (2008). Energetic electron acceleration during multi-island coalescence. *Physics*
483 *of Plasmas*, *15*(10), 102105. doi: 10.1063/1.2996321
484 Russell, C. T., Anderson, B. J., Baumjohann, W., Bromund, K. R., Dearborn, D., Fischer, D., et
485 al. (2016). The magnetospheric multiscale magnetometers. *Space Science Reviews*, *199*(1),
486 189-256. doi: 10.1007/s11214-014-0057-3
487 Shi, Q. Q., Shen, C., Pu, Z. Y., Dunlop, M. W., Zong, Q. G., Zhang, H., et al. (2005).
488 Dimensional analysis of observed structures using multipoint magnetic field measurements:
489 Application to Cluster. *Geophysical Research Letters*, *32*(12). doi: 10.1029/2005GL022454
490 Shi, Q. Q., Shen, C., Dunlop, M. W., Pu, Z. Y., Zong, Q. G., Liu, Z. X., et al. (2006). Motion of
491 observed structures calculated from multi-point magnetic field measurements: Application to
492 Cluster. *Geophysical Research Letters*, *33*(8). doi: 10.1029/2005GL025073

493 Slavin, J. A., Lepping, R. P., Gjerloev, J., Fairfield, D. H., Hesse, M., Owen, C. J., et al. (2003).
494 Geotail observations of magnetic flux ropes in the plasma sheet. *Journal of Geophysical*
495 *Research: Space Physics*, *108*(A1), SMP-10. doi: 10.1029/2002JA009557
496 Sonnerup, B. U., & Scheible, M. (1998). Minimum and maximum variance analysis. *Analysis*
497 *methods for multi-spacecraft data*, *1*, 185-220.
498 Swisdak, M. (2016). Quantifying gyrotropy in magnetic reconnection. *Geophysical Research*
499 *Letters*, *43*(1), 43-49. doi: 10.1002/2015GL066980
500 Tang, C. L., Wang, Y. X., Ni, B., Zhang, J. C., Reeves, G. D., Su, Z. P., et al. (2017). Radiation
501 belt seed population and its association with the relativistic electron dynamics: A statistical
502 study. *Journal of Geophysical Research: Space Physics*, *122*(5), 5261-5276. doi:
503 10.1002/2017JA023905
504 Torbert, R. B., Russell, C. T., Magnes, W., Ergun, R. E., Lindqvist, P. A., LeContel, O., et al.
505 (2016). The FIELDS instrument suite on MMS: Scientific objectives, measurements, and data
506 products. *Space Science Reviews*, *199*(1), 105-135. doi: 10.1007/s11214-014-0109-8
507 Turner, D. L., Cohen, I. J., Michael, A., Sorathia, K., Merkin, S., Mauk, B. H., et al. (2021). Can
508 Earth's magnetotail plasma sheet produce a source of relativistic electrons for the radiation
509 belts?. *Geophysical research letters*, *48*(21), e2021GL095495. doi: 10.1029/2021GL095495
510 Wang, H., Lu, Q., Huang, C., & Wang, S. (2016b). The mechanisms of electron acceleration
511 during multiple X line magnetic reconnection with a guide field. *The Astrophysical Journal*,
512 *821*(2), 84. doi: 10.3847/0004-637X/821/2/84
513 Wang, R., Lu, Q., Nakamura, R., Baumjohann, W., Russell, C. T., Burch, J. L., et al. (2017).
514 Interaction of magnetic flux ropes via magnetic reconnection observed at the magnetopause.

Journal of Geophysical Research: Space Physics, *122*(10), 10-436. doi: 10.1002/2017JA024482

Wang, R., Lu, Q., Nakamura, R., Huang, C., Du, A., Guo, F., et al. (2016a). Coalescence of magnetic flux ropes in the ion diffusion region of magnetic reconnection. *Nature Physics*, *12*(3), 263-267. doi: 10.1038/nphys3578

Xu, Q., Zhou, M., Ma, W., He, J., Huang, S., Zhong, Z., et al. (2023). Electron heating in magnetosheath turbulence: Dominant role of the parallel electric field within coherent structures. *Geophysical Research Letters*, *50*(6), e2022GL102523. doi: 10.1029/2022GL102523

Zank, G. L., Le Roux, J. A., Webb, G. M., Dosch, A., & Khabarova, O. (2014). Particle acceleration via reconnection processes in the supersonic solar wind. *The Astrophysical Journal*, *797*(1), 28. doi: 10.1088/0004-637X/797/1/28

Zhong, Z. H., Lei, G. Y., Zhou, M., Zhang, M., Tang, R. X., Graham, D. B., et al. (2023). Observations of Dynamical Flux Ropes and Active Multiple X-Line Reconnection at Earth's Magnetopause. *Journal of Geophysical Research: Space Physics*, *128*(3), e2022JA031091. doi: 10.1029/2022JA031091

Zhong, Z. H., Tang, R. X., Zhou, M., Deng, X. H., Pang, Y., Paterson, W. R., et al. (2018). Evidence for secondary flux rope generated by the electron Kelvin-Helmholtz instability in a magnetic reconnection diffusion region. *Physical Review Letters*, *120*(7), 075101. doi: 10.1103/PhysRevLett.120.075101

Zhong, Z. H., Zhou, M., Tang, R. X., Deng, X. H., Turner, D. L., Cohen, I. J., et al. (2020). Direct evidence for electron acceleration within ion-scale flux rope. *Geophysical Research Letters*, *47*(1), e2019GL085141. doi: 10.1029/2019GL085141

538 Zhou, M., Berchem, J., Walker, R. J., El-Alaoui, M., Deng, X., Cazzola, E., et al. (2017).
539 Coalescence of macroscopic flux ropes at the subsolar magnetopause: Magnetospheric
540 Multiscale observations. *Physical Review Letters*, *119*(5), 055101. doi:
541 10.1103/PhysRevLett.119.055101
542 Zhou, M., Deng, X. H., & Huang, S. Y. (2012). Electric field structure inside the secondary
543 island in the reconnection diffusion region. *Physics of Plasmas*, *19*(4). doi: 10.1063/1.3700194
544 Zhou, M., El-Alaoui, M., Lapenta, G., Berchem, J., Richard, R. L., Schriver, D., & Walker, R. J.
545 (2018). Suprathermal electron acceleration in a reconnecting magnetotail: Large-scale kinetic
546 simulation. *Journal of Geophysical Research: Space Physics*, *123*(10), 8087-8108. doi:
547 10.1029/2018JA025502
548 Zong, Q. G., Fritz, T. A., Pu, Z. Y., Fu, S. Y., Baker, D. N., Zhang, H., et al. (2004). Cluster
549 observations of earthward flowing plasmoid in the tail. *Geophysical Research Letters*, *31*(18).
550 doi: 10.1029/2004GL020692

Figure 1.

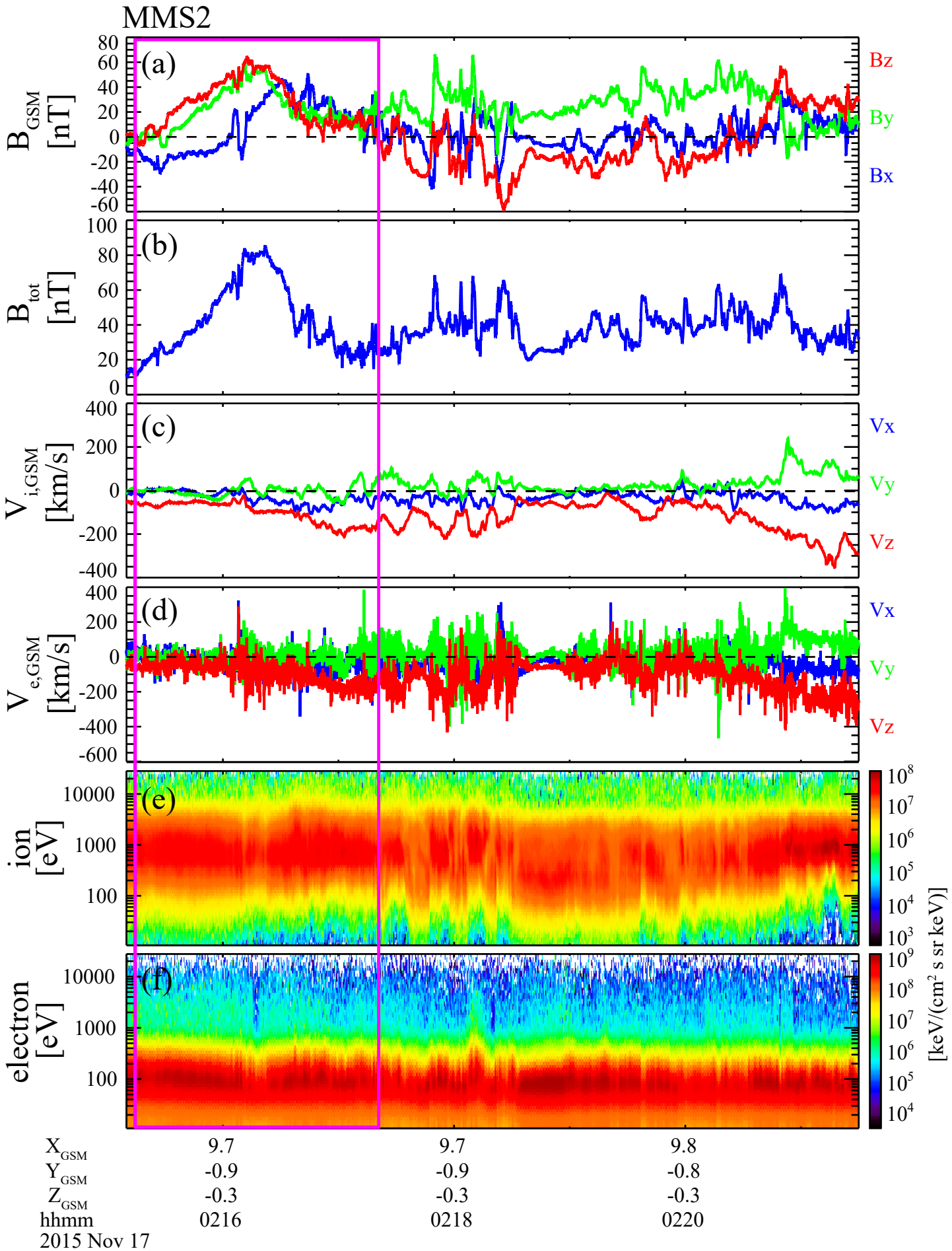
MMS2
(a)
B_GSM [nT]
Bz
By
Bx
(b)
B_tot [nT]
(c)
V_i,GSM [km/s]
Vx
Vy
Vz
(d)
V_e,GSM [km/s]
Vx
Vy
Vz
(e)
ion [eV]
(f)
electron [eV]
[keV/(cm² s sr keV)]
X_GSM 9.7 9.7 9.8
Y_GSM -0.9 -0.9 -0.8
Z_GSM -0.3 -0.3 -0.3
hhmm 0216 0218 0220
2015 Nov 17

Figure 2.

MMS2

MFR1 MFR2 MFR3

(a) B_{GSM} [nT] — Bz, By, Bx

(b) B_{tot} [nT]

(c) $V_{i,GSM}$ [km/s] — Vx, Vy, Vz

(d) $V_{e,GSM}$ [km/s] — Vx, Vy, Vz

(e) $V_{str,GSM}$ [km/s] — Vx, Vy, Vz

(f) T_e [eV] — $T_{e,perp}$, $T_{e,para}$

mms2 X_{gsm} 9.7 -0.9 -0.3 30
mms2 Y_{gsm} 9.7 -0.9 -0.3 00
mms2 Z_{gsm} 9.7 -0.9 -0.3 30
Seconds 0215 0216 0217
2015 Nov 17

(g) B_{LMN} [nT] — B_L, B_M, B_N

(h) $V_{e,LMN}$ [km/s] — V_L, V_M, V_N

(i) $J_{p,LMN}$ [nA/m^2] — J_L, J_M, J_N

(j) E_L [mV/m] — E, $-V_e \times B$, $-V_i \times B$

(k) E_M [mV/m] — E, $-V_e \times B$, $-V_i \times B$

(l) E_N [mV/m] — E, $-V_e \times B$, $-V_i \times B$

(m) $J \cdot (E+V_e \times B)$ [nW/m^3]

(n) $\sqrt{Q}$

Seconds 12.600 .800 13.000 .200 .400 .600 .800 14.000
2015 Nov 17 0217:

Figure 3.

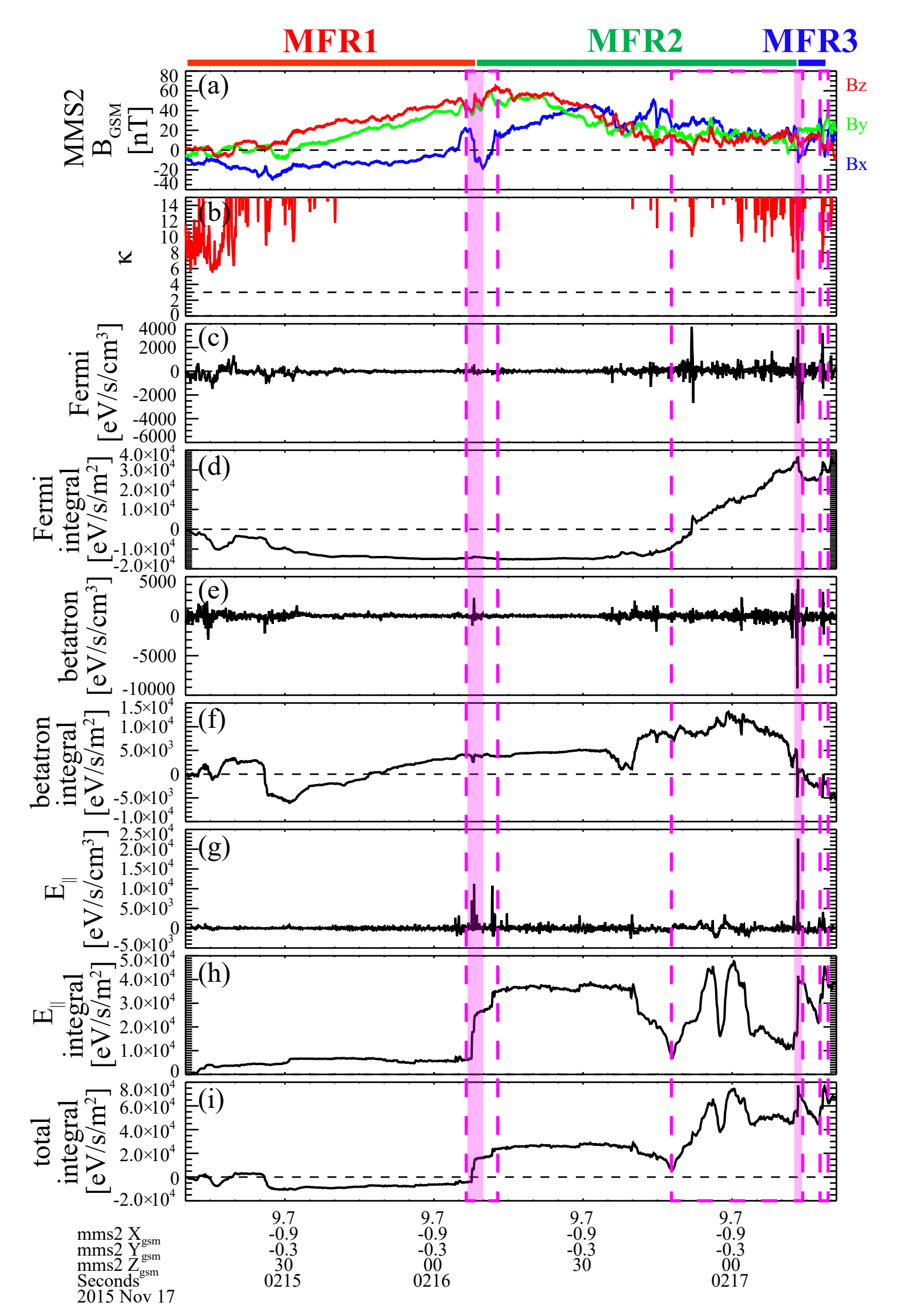
MFR1
MFR2
MFR3
MMS2
B_{GSM} [nT]
Bz
By
Bx
(a)
(b)
κ
(c)
Fermi [eV/s/cm^3]
(d)
Fermi integral [eV/s/m^2]
(e)
betatron [eV/s/cm^3]
(f)
betatron integral [eV/s/m^2]
(g)
$E_{||}$ [eV/s/cm^3]
(h)
$E_{||}$ integral [eV/s/m^2]
(i)
total integral [eV/s/m^2]
mms2 X_{gsm}
mms2 Y_{gsm}
mms2 Z_{gsm}
Seconds
2015 Nov 17
9.7 -0.9 -0.3 30 0215
9.7 -0.9 -0.3 00 0216
9.7 -0.9 -0.3 30
9.7 -0.9 -0.3 00 0217

Figure 4.

Magnetosheath

Small scale MFRs

Jet

MMS

X

Z

Magnetosphere

: Reconnection region

: Fermi acceleration region

: Betatron acceleration region

: $E_{||}$ acceleration region

Figure 5.

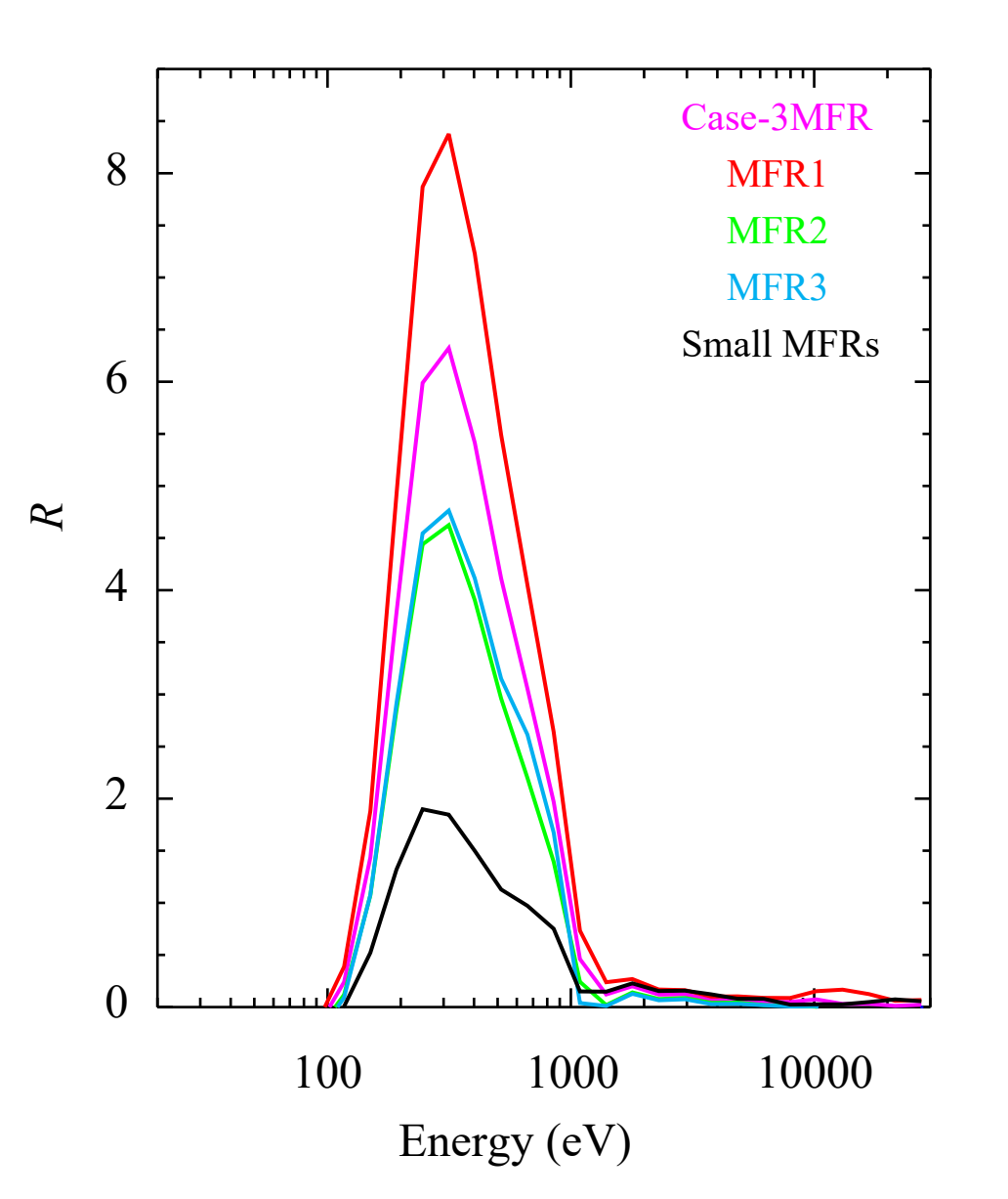
Case-3MFR
MFR1
MFR2
MFR3
Small MFRs
R
0
2
4
6
8
100
1000
10000
Energy (eV)

Figure 6.

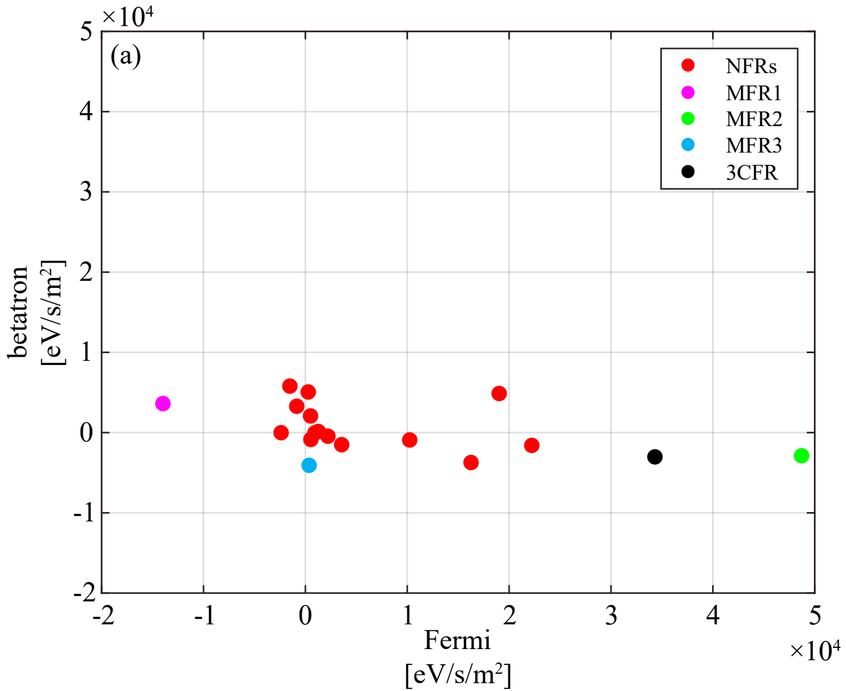
(a)
×10^4
5
4
3
2
1
0
-1
-2
betatron
[eV/s/m²]
-2
-1
0
1
2
3
4
5
×10^4
Fermi
[eV/s/m²]
NFRs
MFR1
MFR2
MFR3
3CFR

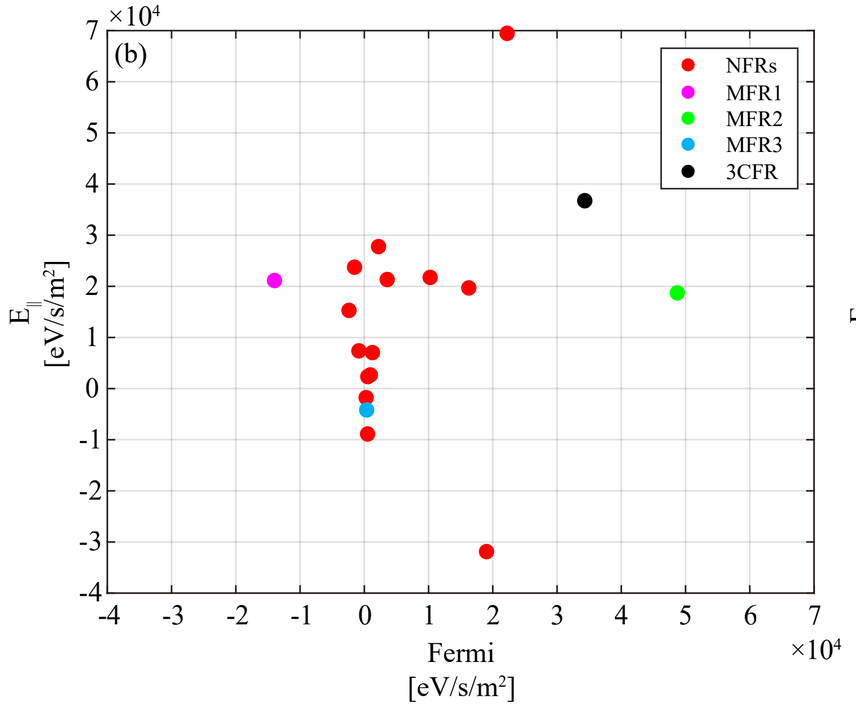
(b)
×10^4
7
6
5
4
3
2
1
0
-1
-2
-3
-4
E∥
[eV/s/m²]
-4
-3
-2
-1
0
1
2
3
4
5
6
7
×10^4
Fermi
[eV/s/m²]
NFRs
MFR1
MFR2
MFR3
3CFR

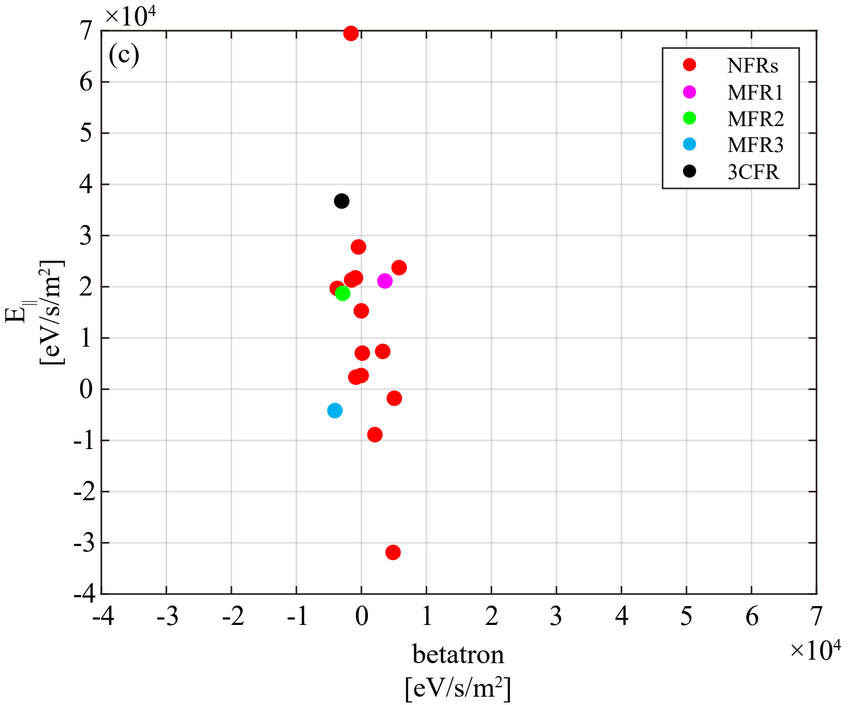
(c)
×10^4
7
6
5
4
3
2
1
0
-1
-2
-3
-4
E∥
[eV/s/m²]
-4
-3
-2
-1
0
1
2
3
4
5
6
7
×10^4
betatron
[eV/s/m²]
NFRs
MFR1
MFR2
MFR3
3CFR